

Single nuclear spin detection and control in a van der Waals material

Xingyu Gao,^{1,*} Sumukh Vaidya,^{1,*} Kejun Li,^{2,3} Zhun Ge,¹ Saakshi Dikshit,⁴ Shimin Zhang,³ Peng Ju,¹ Kunhong Shen,¹ Yuanbin Jin,¹ Yuan Ping,^{3,5,6} and Tongcang Li^{1,4,7,8,†}

¹*Department of Physics and Astronomy, Purdue University, West Lafayette, Indiana 47907, USA*

²*Department of Physics, University of California, Santa Cruz, CA, 95064, USA*

³*Department of Materials Science and Engineering, University of Wisconsin-Madison, 53706, USA*

⁴*Elmore Family School of Electrical and Computer Engineering,
Purdue University, West Lafayette, Indiana 47907, USA*

⁵*Department of Physics, University of Wisconsin-Madison, 53706, USA*

⁶*Department of Chemistry, University of Wisconsin-Madison, 53706, USA*

⁷*Purdue Quantum Science and Engineering Institute,
Purdue University, West Lafayette, Indiana 47907, USA*

⁸*Birck Nanotechnology Center, Purdue University, West Lafayette, Indiana 47907, USA*

(Dated: July 9, 2025)

Optically active spin defects in solids [1, 2] are leading candidates for quantum sensing [3, 4] and quantum networking [5, 6]. Recently, single spin defects were discovered in hexagonal boron nitride (hBN) [7–11], a layered van der Waals (vdW) material. Due to its two-dimensional structure, hBN allows spin defects to be positioned closer to target samples than in three-dimensional crystals, making it ideal for atomic-scale quantum sensing [12], including nuclear magnetic resonance (NMR) of single molecules. However, the chemical structures of these defects [7–11] remain unknown, and detecting a single nuclear spin with an hBN spin defect has been elusive. In this study, we created single spin defects in hBN using ^{13}C ion implantation and identified three distinct defect types based on hyperfine interactions. We observed both $S = 1/2$ and $S = 1$ spin states within a single hBN spin defect. We demonstrated atomic-scale NMR and coherent control of individual nuclear spins in a vdW material, with a π -gate fidelity up to 99.75% at room temperature. By comparing experimental results with density-functional theory calculations, we propose chemical structures for these spin defects. Our work advances the understanding of single spin defects in hBN and provides a pathway to enhance quantum sensing using hBN spin defects with nuclear spins as quantum memories.

Solid-state spin defects have become a leading platform for a wide range of quantum technologies, including multinode quantum networking [5, 6] and quantum-enhanced sensing [3, 4]. These advances are largely driven by the spin-photon quantum interfaces, which utilize optically addressable coherent spins. Despite the success of various spin-photon systems, each material platform has intrinsic limitations, creating trade-offs depending on the specific application [1, 2]. Moreover, spin defects that operate at room temperature are rare. Recently, optically active spin defects in hexagonal boron nitride (hBN), a van der Waals (vdW) material, has garnered vast attention [7–11, 13]. The layered structure of hBN facilitates integration with nanophotonic devices [14] and provides an ideal platform for quantum sensing at the atomic scale [12]. hBN spin defects have been used for sensing magnetic fields [15–17], temperature [15, 16], strain [18], and beyond [19]. However, electron spins in hBN suffer from short spin coherence times [20–22].

Nuclear spins typically exhibit long coherence times thanks to their weak coupling with the local environment, making them ideal candidates for quantum registers [23]. By employing nuclear spins as ancillary qubits,

we can overcome the limitation of electron spin coherence times and enhance the sensitivity of a spin-based quantum sensor [24, 25]. This approach requires the ability to initialize, control, and read out individual nuclear spins [26, 27]. In the context of hBN spin defects, previous experiments used negatively charged boron vacancy (V_B^-) defects to polarize and read out nitrogen nuclear spin ensembles [28–31]. However, these experiments were limited to ensemble-level operations due to the low quantum efficiency of V_B^- defects. Moreover, the relatively short relaxation time of V_B^- electron spins ($T_1 < 20 \mu\text{s}$ at room temperature) restricted the maximum operational time of nuclear spins. Recently discovered single spin defects in hBN [7–11] enabled the readout of individual electron spins in hBN. However, the chemical structures of these single spin defects remain unidentified, and the control of individual nuclear spins in hBN or other vdW materials is still elusive.

In this article, we report the first realization of single nuclear spin detection and control using a carbon-related defect in hBN. Our study reveals three major types of single spin defects in ^{13}C implanted hBN, with remarkably high optically detected magnetic resonance (ODMR) contrasts of up to 200%. Two of these defect types are strongly coupled to nearby ^{13}C nuclear spins. We observe the coexistence of $S = 1$ and $S = 1/2$ states within a single spin defect, though only the $S =$

* These authors contributed equally to this work.

† tcli@purdue.edu

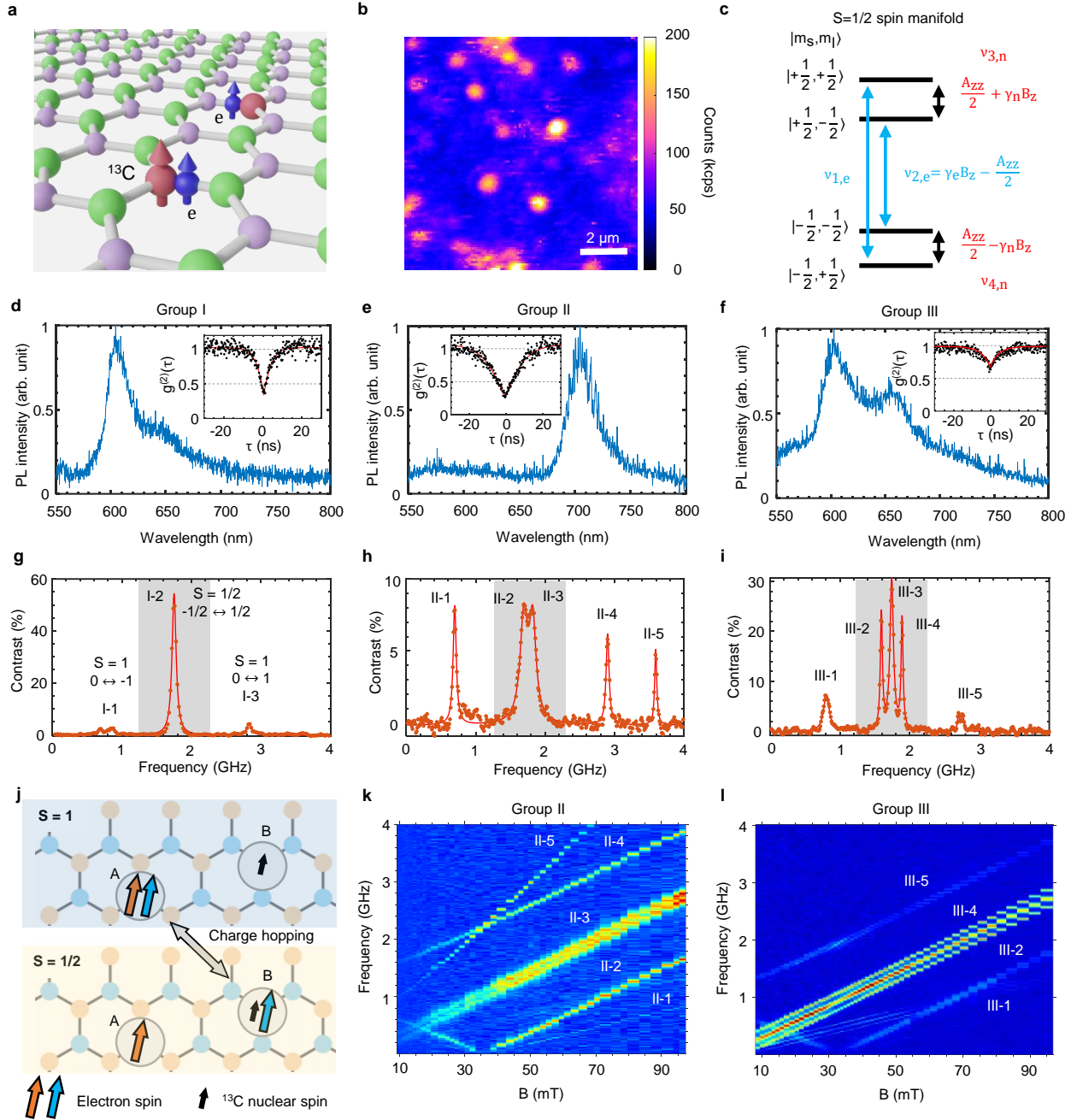


Figure 1. **Observation of three types of single spin defects in hBN.** (a) An illustration of a carbon-related spin defect complex, consisting of an electron spin strongly coupled to a ^{13}C nuclear spin and a nearby, weakly coupled electron spin without strong hyperfine interaction. (b) A PL confocal map showing isolated bright emitters in hBN. Scale bar: $2\ \mu\text{m}$. (c) An energy level diagram of an electron spin $S = 1/2$, coupled to a ^{13}C nuclear spin ($I = 1/2$). A_{zz} is the hyperfine interaction strength. $\nu_{1,e}$ and $\nu_{2,e}$ are the two electron spin transitions. (d)-(f) Optical spectra of Defect 1-3, belonging to Group I-III, respectively. (g)-(i) ODMR spectra of Defects 1-3 under an out-of-plane external magnetic field of 62.5 mT. The number of peaks in the central region (shaded area) differs among Group I-III defects. Within this shaded area, the peaks correspond to the $|-1/2\rangle \leftrightarrow |1/2\rangle$ transitions, with hyperfine structures observed in Groups II and III. Outside the shaded region, the transitions correspond to the $|0\rangle \leftrightarrow |\pm 1\rangle$ transitions. Additionally, the defect in (h) exhibits a $|-1\rangle \leftrightarrow |1\rangle$ double-quantum transition (II-5). (j) An illustration of the spin pair model for explaining the coexistence of $S = 1$ and $S = 1/2$ transitions. (k)-(l) Magnetic field dependent ODMR spectra of Defect 2 in Group II (k), and Defect 3 in Group III (l).

1/2 states exhibit strong coupling to ^{13}C nuclear spins, with coupling strengths reaching up to 300 MHz. The strong hyperfine coupling results in well resolved hyperfine structures, enabling the initialization and readout of single nuclear spins assisted by a defect electron spin. We realize electron-nuclear spin two-qubit gate and coherent control of a ^{13}C nuclear spin, with a nuclear spin π -gate fidelity up to 99.75% at room temperature. We also perform Ramsey and Hahn Echo measurements of the nuclear spin. The dephasing and coherence times of a typical ^{13}C nuclear spin in hBN at room temperature are measured to be $T_2^* = 16.6 \mu\text{s}$ and $T_2 = 162 \mu\text{s}$, respectively. Our density-functional theory calculations suggest that C_B^+C_N^0 donor-acceptor pairs (DAP) and C_BO_N are likely key components for the two types of spin defects with large hyperfine interactions.

Single spin defects in ^{13}C implanted hBN

We create carbon-related spin defects in hBN [8, 9, 11] (Fig. 1) by $^{13}\text{CO}_2$ (99% ^{13}C) ion implantation and thermal annealing (Supplemental Section II). A confocal photoluminescence (PL) map reveals isolated emitters, as depicted in Fig. 1(b). Their optical spectra spread from 570 nm to 700 nm, depending on different defects (Figure 1(d)-(f)). Photon correlation measurements suggest that some defects are single photon emitters ($g^{(2)}(0) < 0.5$). To verify their spin properties, we perform ODMR measurements by toggling the microwave on and off while collecting the emitted photons. The ODMR contrast C is determined by the ratio of photon count rates when the microwave is on (N_{on}) or off (N_{off}): $C = (N_{\text{on}} - N_{\text{off}})/N_{\text{off}} \times 100\%$. In contrast to previous reports of $S = 1/2$ spin defects with only a single resonant peak in ODMR [7–10], we observe three distinct ODMR spectra with multiple resonances (Fig. 1(g)-(i)). The positive contrast indicates that the defects are initialized into a darker state, while we also observe defects with negative contrasts but are rarer (Supplemental Figure S20). These ODMR spectra feature a center branch (shaded areas in Fig. 1(g)-(i)) comprising multiple resonances that are assigned to hyperfine structures, along with additional side resonances located approximately 1 GHz away from the center branch. The high ODMR contrast and brightness yield a typical DC magnetic field sensitivity of $5 \mu\text{T}/\sqrt{\text{Hz}}$ (Methods).

Based on ODMR spectra as shown in Fig. 1(g)-(i), we categorize the spin defects into three major groups, Group I-III, according to the number of peaks in the center branch. Individual peaks are labeled according to their respective defect group. The hyperfine splitting of Group II and III defects are determined to be 130 MHz and 300 MHz, respectively. Notably, the 300 MHz hyperfine splitting is determined by the separation between transitions III-2 and III-4. The additional center peak, III-3, exhibits a different hyperfine structure under weak microwave driving, suggesting that it originates from a

second electron spin. This observation supports the recently proposed spin-pair model, in which a single defect complex hosts two electron spins, separated by several nanometers, that couple differently to the ^{13}C nuclear spins (Fig. 1(j)) [32, 33].

To better understand the spin transitions, we measure the ODMR spectra as a function of out-of-plane magnetic fields (Figure 1(k) and 1(i)). The results reveal an absence of zero-field splitting (ZFS) in the center branch, corresponding to the $|m_s = +1/2\rangle \leftrightarrow |m_s = -1/2\rangle$ transition within the $S = 1/2$ spin manifold (see Supplemental Section IV for experimental verification). In contrast, the side resonances (II-1, II-4, III-1 and III-5) exhibit non-zero ZFS and disperse with a g -factor of 2, confirming that they correspond to the $|m_s = 0\rangle \leftrightarrow |m_s = \pm 1\rangle$ transitions within the $S = 1$ spin manifold. The Hamiltonian of each spin manifold is given by:

$$H = DS_z^2 + E(S_x^2 - S_y^2) + \gamma_e \mathbf{B} \cdot \mathbf{S} + \sum_i \mathbf{S} \cdot \mathbf{A}_i \cdot \mathbf{I}_i + \gamma_n \mathbf{B} \cdot \mathbf{I}_i, \quad (1)$$

where γ_e and γ_n are the electron spin and the nuclear spin gyromagnetic ratios, and \mathbf{B} is the external magnetic field. \mathbf{S} denotes the electronic spin operator with $S = 1$ or $1/2$. D and E together are the ZFS parameters, which are non-zero for the $S = 1$ states but vanish for the $S = 1/2$ states. \mathbf{I}_i denotes the nuclear spin operator for the i -th nuclear spin coupled to the defect electron. Specifically, $I = 1/2$ for ^{13}C nuclear spins, $I = 1$ for ^{14}N nuclear spins, and $I = 3/2$ for ^{11}B nuclear spins. The hyperfine interaction between the electron spin and the i -th nuclear spin is described by the interaction tensor A_i .

The magnetic field dependent ODMR allows us to extract the ZFS parameter D (typically ~ 1 GHz) and E (varies from 100 MHz to 400 MHz) along an out-of-plane quantization axis for the $S = 1$ transitions (Supplementary Figure S3). This is different from the recent observation of a spin-triplet defect with an in-plane quantization axis [11], making our system more favorable for magnetic field alignment. Additionally, an extra peak II-5 of Defect 2 locates at the frequency $\nu_5 = \nu_1 \pm \nu_4$ and has an LAC with II-4 at 37 mT (Supplemental Figure S3), suggesting a double-quantum transition. While previously proposed spin-pair models based on DAP have focused solely on $S = 1/2$ transitions in metastable state (MS) [32, 33], the coexistence of both $S = 1/2$ and $S = 1$ transitions can be well explained by an extended spin-pair model incorporating additional energy levels and transitions (see Methods). The DAP model also accounts for the large variation in PL spectra observed across different defects, despite their similar ODMR signatures [34, 35].

Detection of single ^{13}C nuclear spins in hBN

The well-resolved hyperfine structures enable us to distinguish different defect groups through two-dimensional (2D) mapping of the ODMR contrast at specific microwave driving frequencies. Figure 2 (a)-(c) present the

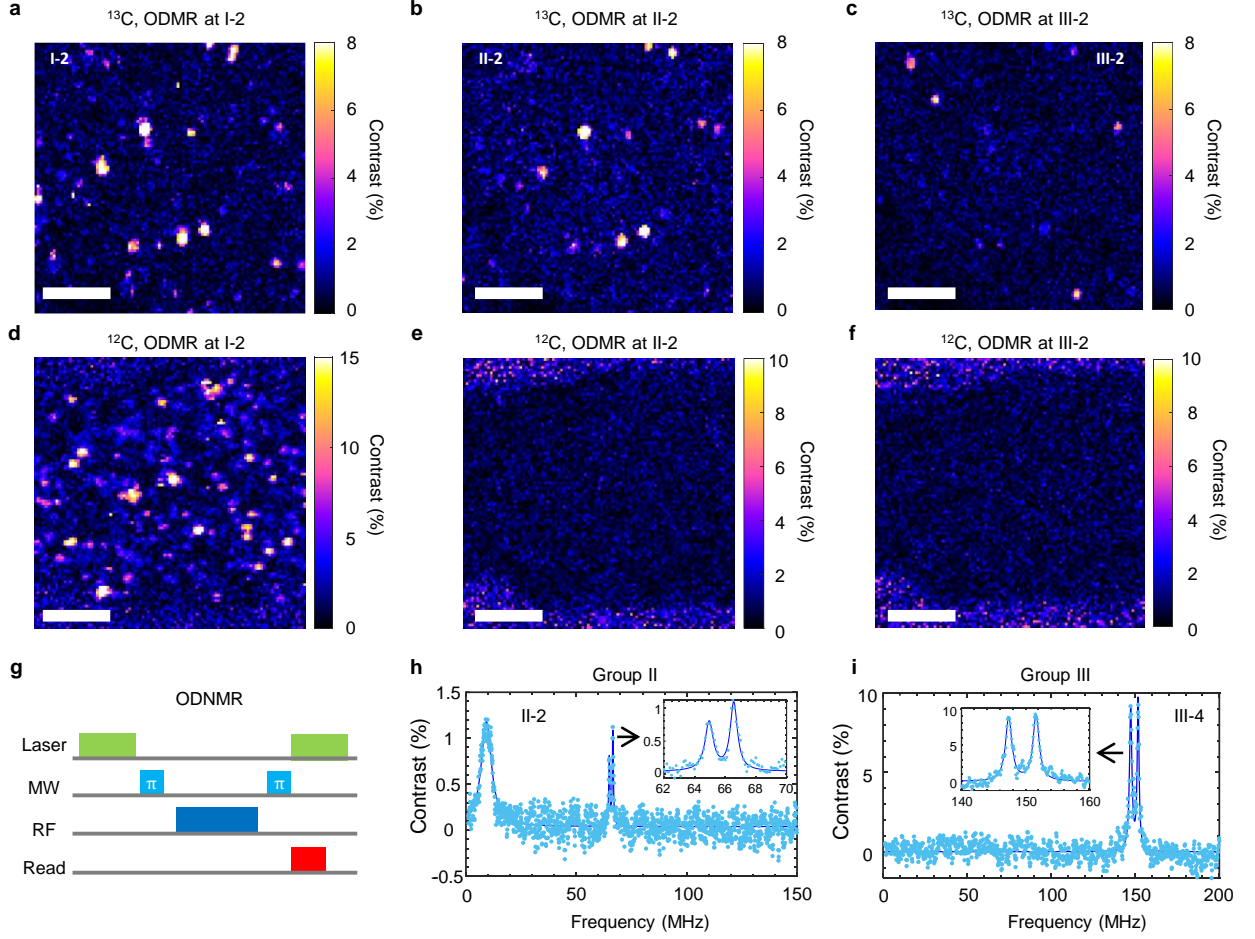


Figure 2. **Optical detection of ^{13}C nuclear spins in hBN.** (a)-(c) ODMR contrast map of ^{13}C implanted hBN by driving a microwave at (a) 2.01 GHz, resonance I-2 of Group I defects; (b) 1.95 GHz, resonance II-2 of Group II defects; and (c) 1.86 GHz, resonance III-2 of Group III defects. (d)-(f) ODMR contrast map of ^{12}C implanted hBN by driving the microwave at (d) I-2, (e) II-2, and (f) III-2. The contrast fluctuation outside the hBN is caused by the low photon counts collected from the background. Scale bars are $5\ \mu\text{m}$. A 71.5 mT magnetic field is applied out-of-plane (perpendicular to the hBN nanosheet). (g) An illustration of the ODNMR sequence. (h) An ODNMR spectrum of Defect 2 by driving the microwave at II-2. (i) An ODNMR spectrum of Defect 3 by driving the microwave at III-4.

ODMR contrast distribution of a ^{13}C -implanted hBN with microwaves resonant at I-2, II-2 and III-2 transitions (Fig. 1(g)-(i)), respectively. All three maps reveal multiple spots with finite contrasts, enabling us to locate Group II and Group III defects. In contrast, no ODMR signal is observed in ^{12}C -implanted hBN when microwaves are applied at the II-2 and III-2 transitions.

Besides ODMR, optically detected nuclear magnetic resonance (ODNMR) (Figure 2(g)) of ^{13}C nuclear spins can provide further insights into the electron-nuclear hyperfine coupling. Here we conduct these measurements at the center branch of Group II and III defects. For both Defect 2 and Defect 3, we observe two closely spaced resonances in ODNMR at approximately half the frequencies of the hyperfine splitting observed in ODMR (Figure 2(h)-(i)). Such a feature verifies the $S = 1/2$ configuration of the defect electron spin for these transitions. For

a $S = 1$ configuration, we expect the ODNMR resonance frequency to be the same as the hyperfine splitting in ODMR. The two-peak structure originates from the external magnetic field and/or a weaker hyperfine coupling to a second electronic spin. We also notice that different nuclear resonance frequencies are obtained when the microwave is applied at III-2 (III-4) and III-3 (Supplemental Figure S17). These features further verify two $S = 1/2$ electron spins are involved in Defect 3.

Coherent control of a ^{13}C nuclear spin in hBN

The well-isolated electron spin transitions at III-2 and III-4 (Fig. 1(i)) enable coherent manipulation of individual electron spin states associated with different nuclear spin states. This capability allows for the initialization,

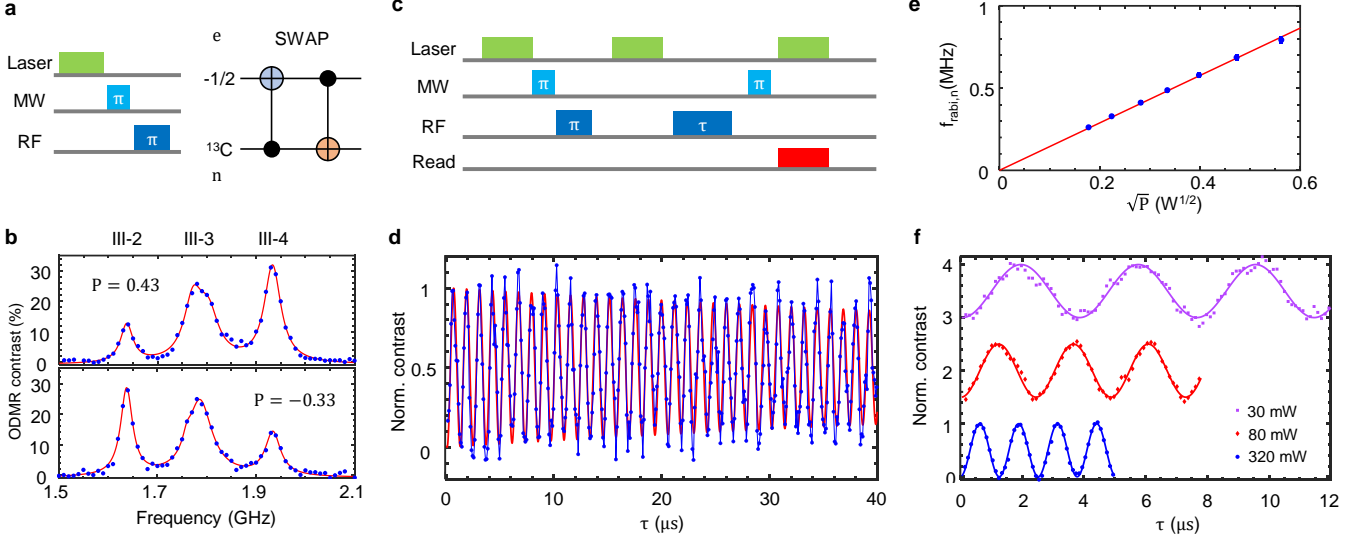


Figure 3. **Initialization and coherent control of a ^{13}C nuclear spin.** (a) An illustration of the pulse sequence (left panel) for nuclear spin initialization. We use a SWAP gate (right panel) to transfer the electron spin polarization to the ^{13}C nuclear spin. (b) ODMR signal after nuclear spin initialization. One of the two peaks (III-2 and III-4) dominates, yielding a nuclear spin polarization of 0.43 (top panel) and -0.33 (bottom panel), depending on the direction of initialization. (c) Pulse sequence for nuclear spin coherent control. (d) An example of nuclear spin Rabi oscillation, persisting for 40 μs without significant decay. The blue curve is the experimental data, and the red curve is fitting. (e) Nuclear spin Rabi frequency as a function of the square root of the RF power. (f) Nuclear spin Rabi oscillations taken at different RF powers: 30 mW (purple squares), 80 mW (Red diamonds), and 320 mW (Blue dots).

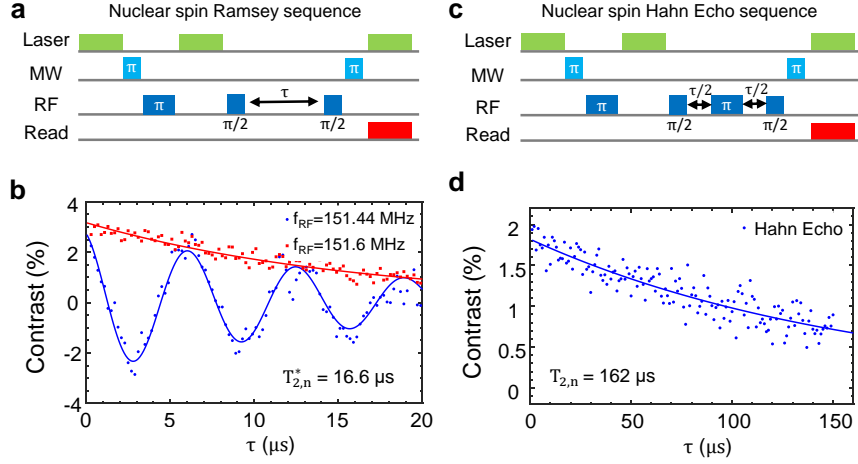


Figure 4. **Spin coherence of a ^{13}C nuclear spin.** (a) The pulse sequence of nuclear spin Ramsey interferometry. (b) The nuclear spin Ramsey fringe. The measurements are performed when the RF frequency is in resonance with the nuclear spin transition (red squares) or slightly detuned from the resonance (blue dots). The fitting of the oscillation showing an inhomogeneous dephasing time of $T_{2,n}^* = 16.6 \mu\text{s}$. (c) The pulse sequence of nuclear spin Hahn Echo. (d) The nuclear spin Hahn Echo measurement shows a slow decay with $T_{2,n} = 162 \mu\text{s}$.

control, and readout of a nuclear spin via the electron spin, without the need for strong magnetic fields or level anticrossing (LAC) [28–31].

To polarize the ^{13}C nuclear spin, we first use a laser pulse to initialize the electron state (assuming $|m_s = -1/2\rangle$). Next, we apply a SWAP gate (Figure 3(a)) to swap the electron spin state and nuclear spin state, after which the nuclear spin is initialized to $|\uparrow\rangle$

(or $|\downarrow\rangle$). To estimate the fidelity of nuclear spin initialization, we measure the electron spin ODMR signal after the SWAP gate and calculate the polarization according to the imbalance between III-2 and III-4 (Figure 3(b)). We determine the nuclear spin polarization to be approximately 43% (-33%) using the equation $P = (\rho_4 - \rho_2)/(\rho_4 + \rho_2)$, where ρ_j represents the amplitude of resonance III-j. A higher nuclear spin polarization

of 60% can be achieved with another defect as shown in Supplemental Figure S18.

For nuclear spin coherent control, we use the protocol depicted in Figure 3(c). After polarizing the nuclear spin, another 10- μ s laser pulse re-initializes the electron spin state. Subsequently, we park the frequency of the selective RF pulse while varying its pulse duration τ . Finally, the nuclear spin state is read out via the spin defect using a selective microwave π pulse and a 5- μ s laser pulse. Figure 3(d) shows the resulting nuclear spin Rabi oscillations. We determine a π -pulse time of 0.6 μ s and a coherence time of 117 μ s by fitting the oscillation contrast $C(\tau)$ to $C(\tau) = a \cdot \sin(\pi\tau/T_\pi + b) \exp(-\tau/T_{Rabi}) + d$, yielding a π -gate fidelity of 99.75% (Methods). The extended operational time for nuclear spins is attributed to the long electron spin relaxation time ($T_{1,e} = 144$ μ s, Supplemental Figure S15) of this carbon-related spin defect, which is an order of magnitude longer than that of V_B^- spin ensembles [28, 29]. By repeating the measurements at different RF powers, we observe a clear power dependence of the oscillations (Figure 3(f)), where the nuclear Rabi frequency is linearly proportional to the amplitude of the RF field (Figure 3(e)).

We further characterize the nuclear spin coherence via Ramsey and Hahn Echo sequences, as illustrated in Figure 4 (a)-(b). In the Ramsey interferometry, when RF pulses are applied exactly in resonance with the nuclear spin transitions, we observe a slow decay in 20 μ s. With a slight detuning of the RF frequency, an additional oscillation is observed alongside the original decay. By fitting the oscillation using the equation $a \cdot \cos(\omega\tau + \phi) e^{-\tau/T_{2,n}^*} + c$, we determine the inhomogeneous dephasing time to be $T_{2,n}^* = 16.6$ μ s and the oscillation frequency to be the same as the detuning. Figure 4(d) shows the exponential decay measured by the nuclear spin Hahn Echo sequence, revealing a nuclear spin coherence time of $T_{2,n} = 162$ μ s. The nuclear spin coherence time is comparable with the electron spin relaxation time $T_{1,e} = 144$ μ s (Supplemental Figure S15), suggesting the measurement is limited by the electronic spin lifetime.

Identifying chemical structures

In addition to providing long-lived spin qubits, nuclear spin magnetic resonance offers valuable insight into identifying defect structures. Here, we perform first-principles calculations of the static properties and hyperfine interaction tensors to enable direct comparison with experimental data. Our calculations suggest that $C_B C_N$ -DAP- L [36] is a likely member of the spin pair responsible for Group II defects (Figure 5(a)). This dimer can exist in two charge states: $C_B^+ C_N^0$ -DAP- L and $C_B^0 C_N^+$ -DAP- L . The positively charged state ($C_B^+ C_N^0$ -DAP- L) has an $S = 1/2$ manifold, and our calculations predict a $^{13}\text{C}_N$ hyperfine coupling of 135 MHz (for $L = 2$). This value closely matches the experimentally observed 130 MHz.

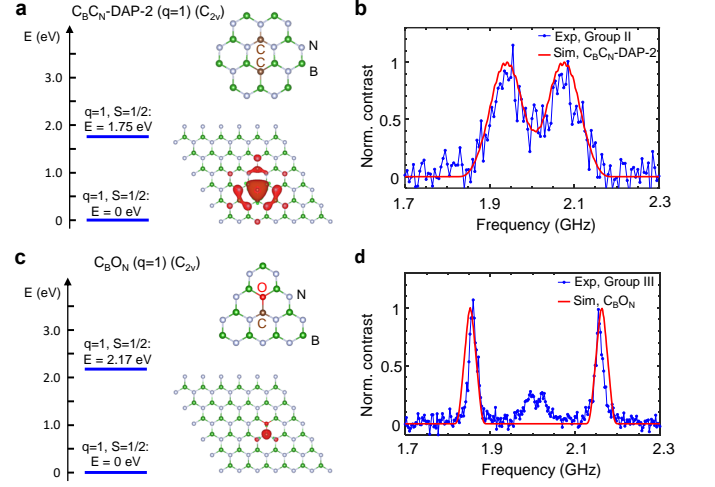


Figure 5. Candidates for the defect members in spin pairs. (a) Chemical structure, spin density and energy-level diagram of the positively charged $C_B^+ C_N^0$ -DAP-2 defect. (b) Simulated ODMR spectrum of the positively charged $C_B^+ C_N^0$ -DAP-2 defect based on the calculated hyperfine coupling parameters. The simulation result (red curve) is compared with the experimental result (blue curve). (c) Chemical structure, electronic wavefunction and energy level diagram of the positively charged $C_B O_N$ defect. (d) Simulated ODMR spectrum of the positively charged $C_B O_N$ defect based on the calculated hyperfine coupling parameters. The simulation result (red curve) is compared with the experimental result (blue curve).

The simulated ODMR spectrum aligns well with the measured ODMR, as shown in Figure 5(b). In addition, the calculated hyperfine coupling for the nearest ^{11}B nuclear spins is 17.6 MHz, resulting in an ODMR resonance at 8.8 MHz, which closely matches the observed ODMR resonance at 9.2 MHz in Figure 2(h). Since the spin density is primarily localized at the C_N site and is barely affected by the distance L , the hyperfine coupling strength remains nearly unchanged for different L values (Supplemental Figure S32).

To account for the observed 300 MHz hyperfine splitting in Group III defects, we consider an oxygen substitution next to the $^{13}\text{C}_B$ site, forming a $C_B O_N$ defect [10] as one member of the spin pair. Oxygen impurities exist in hBN samples [37] and can also be introduced during annealing due to residual oxygen in the vacuum chamber. The positively charged state ($C_B O_N^+$) of this defect hosts a spin-doublet manifold ($S = 1/2$) (Figure 5(c)) with a hyperfine interaction strength $A_{zz} = 314$ MHz, in close agreement with our measured 300 MHz splitting. In Figure 5(d), the simulated ODMR linewidth induced by the nuclear spin bath is 23 MHz, comparable to the 16 MHz linewidth measured under weak microwave driving (Supplemental Figure S13). The central peak (III-3) in Fig. 5(d)) is attributed to a second nearby spin defect.

For both Group II and III defects, the structures discussed above correspond to the defect members in the

spin pairs that exhibit strong hyperfine coupling. We expect a second, nearby donor or acceptor defect, couples to the proposed defect candidates to form a defect DAP complex. The structure of the other defect remains unclear due to lack of characteristic hyperfine features. Further identification of both defect constituents may be possible by using high-purity hBN to suppress intrinsic ^{12}C impurities, combined with higher ^{13}C implantation density. This approach would improve the probability that both defects interact with ^{13}C nuclear spins, enabling more definitive structural assignments.

Conclusion

In conclusion, we report the detection and coherent control of single ^{13}C nuclear spins using single hBN spin defects at room temperature. We find three distinct defect groups in $^{13}\text{CO}_2$ implanted hBN samples, categorized based on their ODMR spectra. We observe both $S = 1/2$ and $S = 1$ spin states within a single hBN spin defect complex, which displays quantum coherence

at room temperature and ODMR contrast up to 200%. In addition, the electronic spin state can be readout using a reasonably long laser pulse of around $5\ \mu\text{s}$, yielding approximately one photon per readout pulse (Supplemental Figure S16) and a single-short spin readout efficiency of $\eta = 0.12$ (see Methods).

Leveraging the control of individual resonances within the well-resolved hyperfine structures, we demonstrate initialization, coherent control and readout of a single ^{13}C nuclear spin using spin defects in Group II (Supplemental Section IV) and Group III. The nuclear spins exhibits coherence times that are orders of magnitudes longer than those of electronic spins in hBN, offering the potential for long-lived quantum registers. The well-resolved hyperfine structure, combined with the high readout efficiency of spin states enabled by the high ODMR contrasts and the extended nuclear spin coherence times, makes this approach promising for achieving single-shot readout of individual nuclear spins [26]. This capability is crucial for implementing quantum error correction protocols in a quantum register [27]. Moreover, the ^{13}C nuclear spin can serve as a quantum memory to enhance quantum sensing with single hBN spin defects.

-
- [1] Mete Atatüre, Dirk Englund, Nick Vamivakas, Sang-Yun Lee, and Joerg Wrachtrup. Material platforms for spin-based photonic quantum technologies. *Nature Reviews Materials*, 3(5):38–51, 2018.
 - [2] Gary Wolfowicz, F Joseph Heremans, Christopher P Anderson, Shun Kanai, Hosung Seo, Adam Gali, Giulia Galli, and David D Awschalom. Quantum guidelines for solid-state spin defects. *Nature Reviews Materials*, 6: 906–925, 2021.
 - [3] Christian L Degen, Friedemann Reinhard, and Paola Cappellaro. Quantum sensing. *Reviews of modern physics*, 89:035002, 2017.
 - [4] Jiangfeng Du, Fazhan Shi, Xi Kong, Fedor Jelezko, and Jörg Wrachtrup. Single-molecule scale magnetic resonance spectroscopy using quantum diamond sensors. *Reviews of Modern Physics*, 96:025001, 2024.
 - [5] Matteo Pompili, Sophie LN Hermans, Simon Baier, Hans KC Beukers, Peter C Humphreys, Raymond N Schouten, Raymond FL Vermeulen, Marijn J Tiggelman, Laura dos Santos Martins, Bas Dirkse, et al. Realization of a multinode quantum network of remote solid-state qubits. *Science*, 372:259–264, 2021.
 - [6] CM Knaut, A Suleymanzade, Y-C Wei, DR Assumpcao, P-J Stas, YQ Huan, B Machielse, EN Knall, M Sutula, G Baranes, et al. Entanglement of nanophotonic quantum memory nodes in a telecom network. *Nature*, 629: 573–578, 2024.
 - [7] Nathan Chejanovsky, Amlan Mukherjee, Jianpei Geng, Yu-Chen Chen, Youngwook Kim, Andrej Denisenko, Amit Finkler, Takashi Taniguchi, Kenji Watanabe, Durga Bhaktavatsala Rao Dasari, et al. Single-spin resonance in a van der Waals embedded paramagnetic defect. *Nature materials*, 20:1079–1084, 2021.
 - [8] Noah Mendelson, Dipankar Chugh, Jeffrey R Reimers, Tin S Cheng, Andreas Gottscholl, Hu Long, Christopher J Mellor, Alex Zettl, Vladimir Dyakonov, Peter H Beton, et al. Identifying carbon as the source of visible single-photon emission from hexagonal boron nitride. *Nature materials*, 20:321–328, 2021.
 - [9] Hannah L Stern, Qiushi Gu, John Jarman, Simone Eizagirre Barker, Noah Mendelson, Dipankar Chugh, Sam Schott, Hoe H Tan, Henning Sirringhaus, Igor Aharonovich, et al. Room-temperature optically detected magnetic resonance of single defects in hexagonal boron nitride. *Nature communications*, 13(1):618, 2022.
 - [10] Nai-Jie Guo, Song Li, Wei Liu, Yuan-Ze Yang, Xiao-Dong Zeng, Shang Yu, Yu Meng, Zhi-Peng Li, Zhao-An Wang, Lin-Ke Xie, et al. Coherent control of an ultra-bright single spin in hexagonal boron nitride at room temperature. *Nature Communications*, 14(1):2893, 2023.
 - [11] Hannah L Stern, Carmem M. Gilardoni, Qiushi Gu, Simone Eizagirre Barker, Oliver FJ Powell, Xiaoxi Deng, Stephanie A Fraser, Louis Follet, Chi Li, Andrew J Ramsay, et al. A quantum coherent spin in hexagonal boron nitride at ambient conditions. *Nature Materials*, 23(10): 1379–1385, 2024.
 - [12] Lingnan Shen, Di Xiao, and Ting Cao. Proximity-induced exchange interaction: A new pathway for quantum sensing using spin centers in hexagonal boron nitride. *The Journal of Physical Chemistry Letters*, 15 (16):4359–4366, 2024.
 - [13] Andreas Gottscholl, Mehran Kianinia, Victor Soltamov, Sergei Orlinskii, Georgy Mamin, Carlo Bradac, Christian Kasper, Klaus Krambrock, Andreas Sperlich, Milos Toth, et al. Initialization and read-out of intrinsic spin defects in a van der Waals crystal at room temperature. *Nature materials*, 19:540–545, 2020.
 - [14] Joshua D Caldwell, Igor Aharonovich, Guillaume Cass-

- abois, James H Edgar, Bernard Gil, and DN Basov. Photonics with hexagonal boron nitride. *Nature Reviews Materials*, 4:552–567, 2019.
- [15] Andreas Gottscholl, Matthias Diez, Victor Soltamov, Christian Kasper, Dominik Krauß, Andreas Sperlich, Mehran Kianinia, Carlo Bradac, Igor Aharonovich, and Vladimir Dyakonov. Spin defects in hBN as promising temperature, pressure and magnetic field quantum sensors. *Nature communications*, 12:4480, 2021.
- [16] AJ Healey, SC Scholten, T Yang, JA Scott, GJ Abrahams, IO Robertson, XF Hou, YF Guo, S Rahman, Y Lu, et al. Quantum microscopy with van der Waals heterostructures. *Nature Physics*, 19:87–91, 2023.
- [17] Mengqi Huang, Jingcheng Zhou, Di Chen, Hanyi Lu, Nathan J McLaughlin, Senlei Li, Mohammed Alghamdi, Dziga Djugba, Jing Shi, Hailong Wang, et al. Wide field imaging of van der Waals ferromagnet Fe_3GeTe_2 by spin defects in hexagonal boron nitride. *Nature communications*, 13:5369, 2022.
- [18] Xiaodan Lyu, Qinghai Tan, Lishu Wu, Chusheng Zhang, Zhaowei Zhang, Zhao Mu, Jesús Zúñiga-Pérez, Hongbing Cai, and Weibo Gao. Strain quantum sensing with spin defects in hexagonal boron nitride. *Nano Letters*, 22: 6553–6559, 2022.
- [19] Sumukh Vaidya, Xingyu Gao, Saakshi Dikshit, Igor Aharonovich, and Tongcang Li. Quantum sensing and imaging with spin defects in hexagonal boron nitride. *Advances in Physics: X*, 8:2206049, 2023.
- [20] Andreas Gottscholl, Matthias Diez, Victor Soltamov, Christian Kasper, Andreas Sperlich, Mehran Kianinia, Carlo Bradac, Igor Aharonovich, and Vladimir Dyakonov. Room temperature coherent control of spin defects in hexagonal boron nitride. *Science Advances*, 7: eabf3630, 2021.
- [21] Ruotian Gong, Guanghui He, Xingyu Gao, Peng Ju, Zhongyuan Liu, Bingtian Ye, Erik A Henriksen, Tongcang Li, and Chong Zu. Coherent dynamics of strongly interacting electronic spin defects in hexagonal boron nitride. *Nature Communications*, 14(1):3299, 2023.
- [22] Roberto Rizzato, Martin Schalk, Stephan Mohr, Jens C Hermann, Joachim P Leibold, Fleming Bruckmaier, Giovanna Salvitti, Chenjiang Qian, Peirui Ji, Georgy V Astakhov, et al. Extending the coherence of spin defects in hBN enables advanced qubit control and quantum sensing. *Nature Communications*, 14(1):5089, 2023.
- [23] MV Gurudev Dutt, L Childress, L Jiang, E Togan, J Maze, F Jelezko, AS Zibrov, PR Hemmer, and MD Lukin. Quantum register based on individual electronic and nuclear spin qubits in diamond. *Science*, 316: 1312–1316, 2007.
- [24] Sebastian Zaiser, Torsten Rendler, Ingmar Jakobi, Thomas Wolf, Sang-Yun Lee, Samuel Wagner, Ville Bergholm, Thomas Schulte-Herbrüggen, Philipp Neumann, and Jörg Wrachtrup. Enhancing quantum sensing sensitivity by a quantum memory. *Nature communications*, 7(1):12279, 2016.
- [25] Nabeel Aslam, Matthias Pfender, Philipp Neumann, Rolf Reuter, Andrea Zappe, Felipe Fávoro de Oliveira, Andrej Denisenko, Hitoshi Sumiya, Shinobu Onoda, Junichi Isoya, et al. Nanoscale nuclear magnetic resonance with chemical resolution. *Science*, 357(6346):67–71, 2017.
- [26] Philipp Neumann, Johannes Beck, Matthias Steiner, Florian Rempp, Helmut Fedder, Philip R Hemmer, Jörg Wrachtrup, and Fedor Jelezko. Single-shot readout of a single nuclear spin. *Science*, 329:542–544, 2010.
- [27] Gerald Waldherr, Yiqing Wang, S Zaiser, M Jamali, T Schulte-Herbrüggen, H Abe, T Ohshima, J Isoya, JF Du, P Neumann, et al. Quantum error correction in a solid-state hybrid spin register. *Nature*, 506:204–207, 2014.
- [28] Xingyu Gao, Sumukh Vaidya, Kejun Li, Peng Ju, Boyang Jiang, Zhujiang Xu, Andres E Llacsahuanga Allica, Kunhong Shen, Takashi Taniguchi, Kenji Watanabe, et al. Nuclear spin polarization and control in hexagonal boron nitride. *Nature Materials*, 21:1024–1028, 2022.
- [29] Ruotian Gong, Xinyi Du, Eli Janzen, Vincent Liu, Zhongyuan Liu, Guanghui He, Bingtian Ye, Tongcang Li, Norman Y Yao, James H Edgar, et al. Isotope engineering for spin defects in van der waals materials. *Nature Communications*, 15:104, 2024.
- [30] T Clua-Provost, A Durand, Z Mu, T Rastoin, J Fraunié, E Janzen, H Schutte, JH Edgar, G Seine, A Claverie, et al. Isotopic control of the boron-vacancy spin defect in hexagonal boron nitride. *Physical Review Letters*, 131: 126901, 2023.
- [31] Shihao Ru, Zhengzhi Jiang, Haidong Liang, Jonathan Kenny, Hongbing Cai, Xiaodan Lyu, Robert Cernansky, Feifei Zhou, Yuzhe Yang, Kenji Watanabe, et al. Robust nuclear spin polarization via ground-state level anti-crossing of boron vacancy defects in hexagonal boron nitride. *Physical Review Letters*, 132:266801, 2024.
- [32] Islay O Robertson, Benjamin Whitefield, Sam C Scholten, Priya Singh, Alexander J Healey, Philipp Reineck, Mehran Kianinia, Gergely Barcza, Viktor Ivády, David A Broadway, Igor Aharonovich, and Jean-Philippe Tetienne. A charge transfer mechanism for optically addressable solid-state spin pairs. *arXiv preprint arXiv:2407.13148*, 2024.
- [33] Raj N Patel, Rebecca EK Fishman, Tzu-Yung Huang, Jordan A Gusdorff, David A Fehr, David A Hopper, S Alex Breitweiser, Benjamin Porat, Michael E Flatté, and Lee C Bassett. Room temperature dynamics of an optically addressable single spin in hexagonal boron nitride. *Nano Letters*, 24:7623–7628, 2024.
- [34] Qinghai Tan, Jia-Min Lai, Xue-Lu Liu, Dan Guo, Yongzhou Xue, Xiuming Dou, Bao-Quan Sun, Hui-Xiong Deng, Ping-Heng Tan, Igor Aharonovich, et al. Donor-acceptor pair quantum emitters in hexagonal boron nitride. *Nano Letters*, 22:1331–1337, 2022.
- [35] Jonathan Pellicciari, Enrique Mejia, John M Woods, Yanhong Gu, Jiemin Li, Saroj B Chand, Shiyu Fan, Kenji Watanabe, Takashi Taniguchi, Valentina Bisogni, et al. Elementary excitations of single-photon emitters in hexagonal boron nitride. *Nature Materials*, 23:1230–1236, 2024.
- [36] Philipp Auburger and Adam Gali. Towards *ab initio* identification of paramagnetic substitutional carbon defects in hexagonal boron nitride acting as quantum bits. *Physical Review B*, 104:075410, 2021.
- [37] Sylvia Xin Li, Takeo Ichihara, Hyeon Park, Guangwei He, Daichi Kozawa, Yi Wen, Volodymyr B Koman, Yuwen Zeng, Matthias Kuehne, Zhe Yuan, et al. Prolonged photostability in hexagonal boron nitride quantum emitters. *Communications Materials*, 4:19, 2023.

Methods

Sample preparation

The hBN thin flakes were tape-exfoliated from a monocrystalline hBN crystal and transferred onto Si/SiO₂ substrates. Then we irradiated the hBN flakes with 2.5 keV ¹³CO₂ (99.0% ¹³C, Sigma-Aldrich) ions with a dose density of 10¹² cm⁻² using a home-built ion implanter. The sample is then annealed at 1000 °C at 10⁻⁵ torr for 2 hours to activate the carbon-related defects. For ODMR measurements, we transferred the hBN flakes to a coplanar waveguide using the standard dry transfer method with propylene carbonate stamps. The waveguide is made of 200 nm thick silver with a 4 nm thick Al₂O₃ layer on top.

Sensitivity of a single spin defect

The ODMR contrast varies between defects and can reach as high as 200% (Supplemental Figure S24). Among the over 100 spin defects investigated, approximately 25 % exhibit a contrast higher than 10 %. A single hBN spin defect in our sample has a typical sensitivity of 5 $\mu\text{T}/\sqrt{\text{Hz}}$ for DC magnetic field sensing, calculated using $(8\pi/3\sqrt{3}) \cdot (1/\gamma_e) \cdot (\Delta\nu/C\sqrt{I})$ [29], where $\Delta\nu$ is linewidth (20 MHz), C is the contrast (30 %) and I is the photon count rate (170 kcts/s). Additionally, while most Group II and Group III defects exhibit stable behaviors under a weak laser excitation ($\leq 15 \mu\text{W}$), the stability of Group I defects varies significantly.

Estimation of nuclear spin polarization

We estimate the polarization of the ¹³C nuclear spin by evaluating the imbalance between III-2 and III-4 in the ODMR spectrum. The ODMR is taken after the SWAP gate to transfer the electron polarization to the ¹³C nuclear spin. By using the fitted relative populations of the hyperfine basis states, the polarization can be calculated by the equation

$$P = \frac{\sum_{m_I} m_I \rho_{m_I}}{I \sum_{m_I} \rho_{m_I}} = \frac{\rho_{1/2} - \rho_{-1/2}}{\rho_{1/2} + \rho_{-1/2}}. \quad (2)$$

Spin readout efficiency

The efficiency of a single-shot spin readout is an important factor to estimate how efficiently one can determine the electronic spin state of a spin defect, which is highly dependent on the defect properties. The readout efficiency is defined by the signal-to-noise ratio from a single readout pulse and can be express as [38]

$$\eta_s = 1/\sigma_s = \left(1 + 2 \frac{\alpha_0 + \alpha_1}{(\alpha_0 - \alpha_1)^2}\right)^{-1/2}. \quad (3)$$

where α_0 and α_1 are the mean numbers of detected photons for a single measurement of the brighter state and darker state, respectively. We estimate the efficiency based on the pulsed ODMR measurements. The pulsed ODMR contrast is 17.5% when we set readout duration

at 5 μs under a $P_{MW}=60 \text{ mW}$ microwave drive. The contrast reaches 28% when $P_{MW}=2 \text{ W}$. For each readout laser pulse, we obtain approximately 0.9 photon from the darker state under the 15 μW laser pumping. These yield the efficiency of 0.08 and 0.12 for $P_{MW}=60 \text{ mW}$ and $P_{MW}=2 \text{ W}$, respectively. See details in Supplemental Section IV.

Gate fidelity

For Rabi oscillations limited by a pure dephasing process, we can write the π -gate fidelity as $F_\pi = 0.5(1 + \exp(-1/Q_\pi))$, where $Q_\pi = T_{Rabi}/T_\pi$ is the quality factor of a π gate [39]. We extract the coherence time and π -gate time of nuclear spin Rabi by fitting the results in Figure 3 to the function $C(\tau) = a \cdot \sin(\pi\tau/T_\pi + b) \cdot \exp(-\tau/T_{Rabi}) + d$, where $C(\tau)$ is the signal contrast of Rabi. As a results, we obtain a $F_{\pi,n} = 99.75\%$ π -gate fidelity, with $T_{\pi,n} = 0.60 \mu\text{s}$ and $T_{Rabi,n} = 117 \mu\text{s}$. Similarly, we also estimate the electronic spin π -gate fidelity to be 96.2%, using the same defect and transition in the nuclear spin control experiments.

Density-functional theory calculations

We use Quantum Espresso (QE) [40], an open-source plane-wave software, to perform the density-function theory (DFT) calculation. Both the Perdew-Burke-Ernzerhof (PBE) functional and the Heyd-Scuseria-Ernzerhof (HSE) hybrid functional (the factor of 0.32 for Fock exchange) [41, 42] are employed for the exchange-correlation interaction. We use Optimized Norm-Conserving Vanderbilt (ONCV) pseudopotential [43, 44] for the calculations of excitation energy, and the GIPAW pseudopotential [45] for the calculation of hyperfine interaction parameters and zero-field splitting (ZFS). We set the kinetic energy cutoff to be 55 Ry, which is adequate for converging the relevant properties. Geometry optimizations are carried out with a force threshold of 0.001 Ry/Bohr. We select the $6 \times 6 \times 1$ or higher supercell size of hBN for the calculations of hyperfine parameter and excitation energies. For these calculations, we sample a k-point mesh of $3 \times 3 \times 1$ for the calculation of excitation energies [46], and Γ point for the hyperfine parameters and ZFS [28, 46]. We calculate the zero-phonon line (ZPL) by the constraint occupation DFT (CDFT) method [47], the hyperfine parameters using the QE-GIPAW code [48], the ZFS by using the ZFS code [46], and we cross compare results between ZFS code and the PyZFS code [49]. The key results are summarized in Supplemental Table S2-S3.

Simulation of ODMR spectrum

The continuous wave (cw) ODMR spectra shown in Figure 5 are simulated using the MATLAB toolbox EASYSPIN [50] based on data from the *ab initio* calculations. EASYSPIN also takes the nuclear Zeeman and quadrupole interaction into account. Therefore, the cw ODMR linewidth can be determined according to the hyperfine couplings with the most abundant nuclear-spin-active isotopes: ¹³C, ¹¹B and ¹⁴N. In our simulation, we

consider a ^{13}C nuclear spin, ten nearest ^{11}B nuclear spins and two proximate ^{14}N nuclear spins. The other nuclei, located further away, couple more weakly to the electron, scaling with $\propto 1/r^3$ (where r is the distance from the central carbon site), and thereby have a negligible effect on the ODMR linewidth.

Spin pair model

The $S = 1$ transitions are consistently observed alongside the $S = 1/2$ transitions within the same emitters. To explain the coexistence of both spin transitions in ODMR, we employ a weakly coupled spin-pair model [32, 33] and perform numerical simulations to investigate the underlying mechanism.

Extended Data Figure 1 (a) provides a simplified representation of the spin-pair model, consisting of two independent defects (Defect A and B), separated by ≥ 1 nm, forming a defect complex. This complex hosts two unpaired electrons that establish different internal charge states depending on their spatial occupancy. When both electrons are localized on the same defect (Defect A), they form a closed-shell spin singlet GS with a metastable spin triplet state ($S = 1$), which can be accessed through laser excitation and intersystem crossing (ISC) transitions (left panel in Extended Data Figure 1 (b)). This state corresponds to a strongly coupled spin-pair charge state and explains the $S = 1$ transitions.

Alternatively, laser excitation can induce charge hopping that transfers one electron from Defect A to Defect B, forming a weakly coupled defect pair. In this configuration, each defect hosts a single electron ($S = 1/2$), as illustrated in the right panel of Extended Data Figure 1 (b). This spin-dependent charge hopping yields a corresponding spin-dependent PL signal [32].

The actual GS, which is also the optically active state, is determined by the lowest-energy charge configuration and depends on the specific defect species and the local Fermi energy level. We considered two possible energy level configurations (Supplementary Section XII), with Extended Data Figure 1(c) depicting the most likely scenario. In the most stable charge state, both electrons occupy the same defect site, yielding an $S = 0$ GS and a metastable $S = 1$ state. Laser excitation can then generate a metastable spin-pair charge state by promoting transitions from the $S = 1$ to the $S = 1/2$ manifold. The pronounced asymmetry in the Rabi oscillations, reflected by an increasing contrast baseline in both $S = 1/2$ and $S = 1$ transitions, strongly supports the metastable nature of these spin manifolds.

In the presence of a ^{13}C nuclear spin, the defect electron spins can couple to the nuclear spin via hyperfine

interactions, which vary across different charge states. In the weakly coupled spin-pair state, the nuclear spin is primarily coupled to a single electron spin at Defect A. This is consistent with our experimental observations, where hyperfine coupling constants A_{zz} of 130 MHz and 300 MHz were measured for Group II and Group III defects, respectively.

Given their distinct hyperfine features, Group II and Group III defects are likely to have more well-defined and deterministic structures. In contrast, Group I defects, lacking hyperfine splitting, may include a range of chemical configurations: either similar to Group II and III defects (but involving ^{12}C instead of ^{13}C) or very different chemical structures. This structural variability may account for the broader range of stability observed in Group I defects, whereas Group II and III defects tend to exhibit more consistent and stable behavior under experimental conditions.

Simulation of spin photodynamics

Based on the possible energy level models, we numerically simulate the spin photodynamics using the Lindblad master equation:

$$\dot{\rho} = -i[H, \rho(t)] + \sum_k \Gamma_k \left[L_k \rho(t) L_k^\dagger - \frac{1}{2} \{ L_k^\dagger L_k, \rho(t) \} \right], \quad (4)$$

where $\rho(t)$ is the time-dependent density matrix, Γ_k represents transition rates, and L_k are the associated Lindblad operators. This simulation allows us to predict PL signals in both CW ODMR and pulsed Rabi experiments (see details in Supplementary Information).

In the CW ODMR simulation, we use the full Hamiltonian, which includes the optical manifold, spin-pair states, and spin-triplet states. For Model 1, where the GS is a spin singlet ($S = 0$), the Hamiltonian is written as:

$$H = H_{\text{pair}} \oplus H_{m,S1} \oplus H_{eg} = \begin{pmatrix} H_{\text{pair}}^{8 \times 8} & & \\ & H_{m,S1}^{6 \times 6} & \\ & & H_{eg}^{4 \times 4} \end{pmatrix} \quad (5)$$

where H_{eg} , $H_{m,S1}$, and H_{pair} describe the optical manifold, the spin $S=1$ MS and the spin-pair state, respectively (see detailed expressions in Supplementary Information). For each subspace, we consider a ^{13}C nuclear spin coupled via hyperfine interaction. The full Hamiltonian is a direct sum of individual spin manifolds, meaning there is no coherent interaction between them. Instead, they are connected via incoherent transitions described by the Lindblad operators L_k .

-
- [38] David A Hopper, Henry J Shulevitz, and Lee C Bassett. Spin readout techniques of the nitrogen-vacancy center in diamond. *Micromachines*, 9:437, 2018.
- [39] Romain Debroux, Cathryn P Michaels, Carola M Purser,

- Noel Wan, Matthew E Trusheim, Jesús Arjona Martínez, Ryan A Parker, Alexander M Stramma, Kevin C Chen, Lorenzo De Santis, et al. Quantum control of the tin-vacancy spin qubit in diamond. *Physical Review X*, 11:

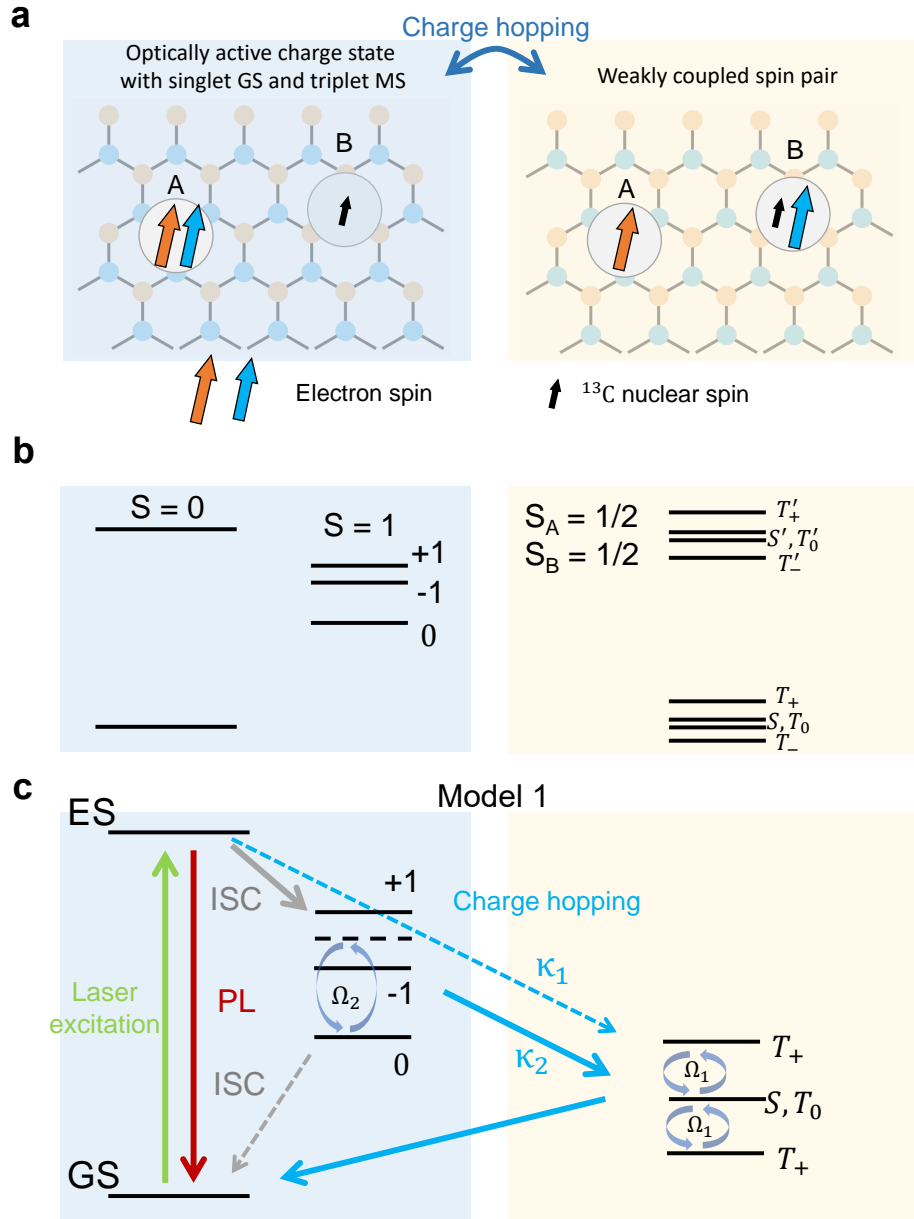
- 041041, 2021.
- [40] Paolo Giannozzi, Stefano Baroni, Nicola Bonini, Matteo Calandra, Roberto Car, Carlo Cavazzoni, Davide Ceresoli, Guido L Chiarotti, Matteo Cococcioni, Ismaila Dabo, Andrea Dal Corso, Stefano de Gironcoli, Stefano Fabris, Guido Fratesi, Ralph Gebauer, Uwe Gerstmann, Christos Gougousis, Anton Kokalj, Michele Lazzeri, Layla Martin-Samos, Nicola Marzari, Francesco Mauri, Riccardo Mazzarello, Stefano Paolini, Alfredo Pasquarello, Lorenzo Paulatto, Carlo Sbraccia, Sandro Scandolo, Gabriele Scalzero, Ari P Seitsonen, Alexander Smogunov, Paolo Umari, and Renata M Wentzcovitch. QUANTUM ESPRESSO: A Modular and Open-Source Software Project for Quantum Simulations of Materials. *J. Phys.: Condens. Matter*, 21:395502, sep 2009.
 - [41] Jochen Heyd, Gustavo E Scuseria, and Matthias Ernzerhof. Hybrid Functionals Based on a Screened Coulomb Potential. *J. Chem. Phys.*, 118:8207–8215, 2003. doi:10.1063/1.1564060.
 - [42] Jochen Heyd, Gustavo E. Scuseria, and Matthias Ernzerhof. Erratum: “Hybrid functionals based on a screened Coulomb potential” [*J. Chem. Phys.* 118, 8207 (2003)]. *The Journal of Chemical Physics*, 124:219906, 06 2006. ISSN 0021-9606. doi:10.1063/1.2204597.
 - [43] D. R. Hamann. Optimized Norm-Conserving Vanderbilt Pseudopotentials. *Phys. Rev. B*, 88:085117, aug 2013.
 - [44] Martin Schlipf and François Gygi. Optimization Algorithm for the Generation of ONCV Pseudopotentials. *Comput. Phys. Commun.*, 196:36–44, 2015.
 - [45] Christian Tantardini, Alexander G Kvasninin, and Davide Ceresoli. Gipaw pseudopotentials of d elements for solid-state nmr. *Mater.*, 15:3347, 2022.
 - [46] Tyler J Smart, Kejun Li, Junqing Xu, and Yuan Ping. Intersystem Crossing and Exciton–Defect Coupling of Spin Defects in Hexagonal Boron Nitride. *npj Comput. Mater.*, 7:1–8, 2021. doi:10.1038/s41524-021-00525-5.
 - [47] M Mackoitis-Sinkevičienė, Marek Maciaszek, Chris G Van de Walle, and Audrius Alkauskas. Carbon Dimer Defect as a Source of the 4.1 eV Luminescence in Hexagonal Boron Nitride. *Appl. Phys. Lett.*, 115:212101, 2019.
 - [48] Nicola Varini, Davide Ceresoli, Layla Martin-Samos, Ivan Girotto, and Carlo Cavazzoni. Enhancement of dft-calculations at petascale: nuclear magnetic resonance, hybrid density functional theory and car–parrinello calculations. *Comput. Phys. Commun.*, 184:1827–1833, 2013.
 - [49] He Ma, Marco Govoni, and Giulia Galli. PyZFS: A Python Package for First-Principles Calculations of Zero-Field Splitting Tensors. *J. Open Source Softw.*, 5:2160, 2020. doi:10.21105/joss.02160.
 - [50] Stefan Stoll and Arthur Schweiger. Easyspin, a comprehensive software package for spectral simulation and analysis in epr. *Journal of magnetic resonance*, 178:42–55, 2006.

ACKNOWLEDGMENTS

T.L. acknowledges the support by the Gordon and Betty Moore Foundation, grant DOI 10.37807/gbmf12259, and the National Science Foundation grant PHY-2409607. The investigation of the spin pair model was supported by the U.S. Department of Energy, Office of Science, Office of Basic Energy Sciences through QuPIDC Energy Frontier Research Center under award Number DE-SC0025620. Y.P. acknowledges the support by the National Science Foundation under grant no. DMR2143233. The *ab initio* calculations used resources of the Scientific Data and Computing Center, a component of the Computational Science Initiative, at Brookhaven National Laboratory under Contract No. DE-SC0012704, the Lux Supercomputer at UC Santa Cruz, funded by NSF MRI Grant No. AST 1828315, the National Energy Research Scientific Computing Center (NERSC), a U.S. Department of Energy Office of Science User Facility operated under Contract No. DE-AC02-05CH11231, and the Extreme Science and Engineering Discovery Environment (XSEDE), which is supported by National Science Foundation Grant No. ACI-1548562.

AUTHOR CONTRIBUTIONS

T.L. and X.G. conceived and designed the project. X.G., S.V., K.S. and Y.J. built the setup. K.L. and S.Z. performed the *ab initio* calculations. P.J. fabricated microwave waveguides. S.V. and S.D. performed the ion implantation and thermal annealing on the hBN samples. X.G. and S.V. performed measurements. X.G. and Z.G. performed the numerical simulation. X.G., S.V., T.L., K.L. and Y.P. analyzed the results. T.L. and Y.P. supervised the project. All authors contributed to the writing of the manuscript.



Extended Data Figure 1. **Spin pair model.** (a) Two possible electron configurations of a spin defect complex in different internal charge states. (b) The energy levels of internal charge states according to the DFT prediction. When two electrons occupy the same defect site (left panel), it forms a singlet GS and ES as well as a triplet MS. When two electrons locate at different defect sites (right panel), each form a $S = 1/2$ state and they are weakly coupled via dipolar interaction, forming a spin $S = 1/2$ pair. (c) A proposed energy level diagram for explaining the coexistence of the $S = 1/2$ and $S = 1$ ODMR transitions.